Nonequilibrium transport and the fluctuation theorem in the thermodynamic behaviors of nonlinear photonic systems

Yang Liu,[1] Jincheng Lu,[2] Zhongfei Xiong,[3] Fan O. Wu,[4] Demetrios Christodoulides,[5] Yuntian Chen,[3] and Jian-Hua Jiang[6,7,8,1,*]

[1]*School of Physical Science and Technology & Collaborative Innovation Center of Suzhou Nano Science and Technology, Soochow University, 1 Shizi Street, Suzhou 215006, China*

[2]*Key Laboratory of Efficient Low-carbon Energy Conversion and Utilization of Jiangsu Provincial Higher Education Institutions, School of Physical Science and Technology, Suzhou University of Science and Technology, Suzhou 215009, China*

[3]*School of Optical and Electronic Information, Huazhong University of Science and Technology, Wuhan 430074, China*

[4]*CREOL, College of Optics and Photonics, University of Central Florida, Orlando, Florida 32816-2700, USA*

[5]*Ming Hsieh Department of Electrical and Computer Engineering, University of Southern California, Los Angeles, California 90089, USA*

[6]*School of Biomedical Engineering, Division of Life Sciences and Medicine, University of Science and Technology of China, Hefei 230026, China*

[7]*Suzhou Institute for Advanced Research, University of Science and Technology of China, Suzhou 215123, China*

[8]*School of Physical Sciences, University of Science and Technology of China, Hefei 230026, China*

(Received 6 April 2024; accepted 6 January 2025; published 23 January 2025)

Nonlinear multimode optical systems have attracted substantial attention due to their rich physical properties. Complex interplay between the nonlinear effects and mode couplings makes it difficult to understand the collective dynamics of photons. Authors of recent studies have shown that such collective phenomena can be effectively described by Rayleigh-Jeans thermodynamics theory, which is a powerful tool for the study of nonlinear multimode photonic systems. These systems, in turn, offer a compelling platform for investigating fundamental issues in statistical physics, attributed to their tunability and the ability to access negative temperature regimes. However, to date, a theory for nonequilibrium transport and fluctuations is yet to be established. Here, we employ full counting statistics theory to study the nonequilibrium transport of particles and energy in nonlinear multimode photonic systems in both positive and negative temperature regimes. Furthermore, we discover that, in situations involving two reservoirs of opposite temperatures and chemical potentials, an intriguing phenomenon known as the loop current effect can arise, wherein the current in the positive energy sector runs counter to that in the negative energy sector. In addition, we numerically confirm that the fluctuation theorem remains applicable in optical thermodynamics systems across all regimes, from positive temperatures to negative ones. Our findings closely align with numerical simulations based on first-principles nonlinear wave equations. In this paper, we seek to deepen the understanding of irreversible nonequilibrium processes and statistical fluctuations in nonlinear many-body photonic systems which will enhance our grasp of collective phenomena of photons and foster a fruitful intersection between optics and statistical physics.

DOI: 10.1103/PhysRevResearch.7.013084

I. INTRODUCTION

The emergence of thermodynamic behaviors in many-body systems is remarkable in the sense that the huge gap between deterministic dynamics and statistical thermodynamics is still not filled after centuries of study. In fact, such a topic has recently attracted research interest again, thanks to the appearance of several systems where the many-body dynamics can be computed numerically [1–6]. One of these systems is the interacting bosonic system. When the interaction is not too strong, the system tends to reach equilibrium states with emergent thermodynamic behaviors that can be tuned by microscopic properties, such as the dispersion, as well as macroscopic properties, such as the total energy and particle number. Such tunable emergent thermodynamic behaviors provide promising opportunities for the study of the fundamental issues in statistical thermodynamics.

One prototype is the multimode optical systems (MMOSs) in various lattices which offer an extremely vigorous platform to study the collective phenomena of photons. Over the past decades, MMOSs have been investigated extensively in their linear optical properties such as transmission in the presence of disorders [7–9], photonic topological phenomena [10–15] ranging from the quantum Hall-like effects [16–21] to Dirac and Weyl physics [22–26], and non-Hermitian effects [27–29]. Meanwhile, nonlinear effects in MMOSs such as the parametric instabilities [30–33], spatiotemporal mode-locking [34,35], and the multimode solitons [36] have also been

*Contact author: jhjiang3@ustc.edu.cn

explored, revealing intriguing phenomena that are unavailable in single-mode or few-mode optical systems. These linear and nonlinear effects are also promising for various applications in photonics.

Indeed, there are interesting phenomena in nonlinear multimode optical systems (NLMMOSs) that can be related to thermodynamics. It was observed recently that, in nonlinear multimode optical fibers driven by the Kerr nonlinear effect, the optical power in many optical modes at the input can automatically evolve to an output state that favors only a few modes. This phenomenon, known as the *beam self-cleaning mechanism* [32,37,38], was recently revealed as a manifestation of the optical thermalization effect [39,40]. The underlying physics is that the thermalization process reshapes the initial distribution to a Rayleigh-Jeans distribution that is pronounced only for a few modes. It is worth noting that the emergent Rayleigh-Jeans distribution contains an effective temperature and a chemical potential that can be largely tuned by the total energy and particle number of the system as well as the couplings between the modes [41–48]. Under certain conditions, even negative temperatures can emerge, as observed in recent experiments [49,50]. Moreover, unlike in classical black-body radiation where the chemical potential is always zero, here, the chemical potential is often nonzero, as constrained by the total photon number. These abnormal aspects enable intriguing transport phenomena in NLMMOSs which are yet to be explored.

In the limit that only a single mode is dominant at the steady-state distribution, the phenomenon is also known as Rayleigh-Jeans condensation [51–55]. For instance, in the positive temperature regime, by keeping the total photon number conserved and decreasing the optical temperature, the optical chemical potential increases, until it reaches the photon energy of the lowest fundamental mode. At such a critical point, the denominator of the Rayleigh-Jeans distribution vanishes [55]. By further decreasing the optical temperature, Rayleigh-Jeans condensation can emerge [51–55]. There are subtle differences between the well-known quantum Bose-Einstein condensation and classical Rayleigh-Jeans condensation. For instance, in a multimode optical fiber system with a parabolic potential, the condensate distribution decreases linearly with the temperature for Rayleigh-Jeans condensation, while it decreases quadratically for Bose-Einstein condensation [55]. Although for both types of condensation the specific heat diverges at the critical temperature, at lower temperatures, the specific heat behaves differently for these two condensations as well [55]. Thus, Rayleigh-Jeans thermalization and condensation considerably enrich the statistical properties of photons. From this aspect, NLMMOSs offer an excellent platform for the study of the statistical physics of photons, as they give access to realms that are not available in other experimental systems. Considering the tunability of such optical systems and the convenience in optical excitation and measurements, the emergent statistical physics of photons in NLMMOSs is a promising direction for exploring fundamental phenomena.

Although the thermodynamic theory for photons in NLMMOSs has been established recently [41,46,56], the theory and experiments for nonequilibrium transport remain largely unexplored [57]. Transport and fluctuations are fundamental phenomena when multiple NLMMOSs exchange energy and particles with each other. In this paper, we promote the theory for nonequilibrium transport and fluctuations from two complementary approaches. We use the full counting statistics (FCS) theory based on the quantum master equation to study the particle transport and fluctuations between two NLMMOSs. In parallel, we employ the nonlinear Schrödinger equation to numerically simulate the photon dynamics in the combined system. Such numerical simulation can provide the transport current and its fluctuation dynamics in the system which can be used to extract the average current and the current statistics. These properties are then compared with the theoretical results from FCS theory. We find reasonable agreement between the two approaches in studying the photon transport and fluctuations, although they have very different starting points. We then use these two approaches to study transport and fluctuations in various regimes. These complementary approaches can also be used to verify the fluctuation theorem in the negative temperature regime. Remarkably, we find that the fluctuation theorem holds even for such a negative temperature regime as supported by various numerical simulations. The heat exchange fluctuation theorem [58,59] is confirmed for both positive and negative temperatures by considering transport between two NLMMOSs coupled by a cross-phase modulation (XPM) mechanism. In this paper, we pave the way toward a comprehensive nonequilibrium statistical physics theory for nonlinear photonic systems.

II. THERMODYNAMIC THEORY FOR PHOTONS IN NLMMOSs

We would like to first introduce two examples of optical thermodynamics in NLMMOSs (Fig. 1). The first example is arrays of cavities or waveguides [60–65]. As shown in Fig. 1(b), a two-dimensional (2D) array of coupled ring cavities can serve as highly tunable NLMMOSs. Here, both the lattice structure and the mode couplings can be tuned by the geometry of the system, while the nonlinearity can be tuned by the materials that form the system. The second example is nonlinear multimode optical fibers which are characterized by refractive index profiles $n(x, y)$ that guide the propagation of photons along the z direction (such a direction is often regarded as the time evolution axis in Schrödinger's equation). It has been revealed that chaotic nonlinear dynamics in this type of system can lead to thermalization effects (e.g., the emergent Rayleigh-Jeans distribution and the mode self-cleaning effect) [66–68]. It is also worth noting that NLMMOSs can be divided into two types, differing by whether the time dimension is real or a synthetic one (e.g., the propagation along the z direction). The first type includes coupled microcavities or resonators where the optical modes evolve with time. The second type includes coupled optical waveguides where the optical modes propagate along the z direction, and their propagation constants play the role of energy. These two types of optical systems have similar behaviors, and the underlying physics discussed in this paper applies to both. Finally, we also remark that, although there are many similarities between the ultracold atomic gases in optical lattice and photons in NLMMOSs, there are a few aspects that make the

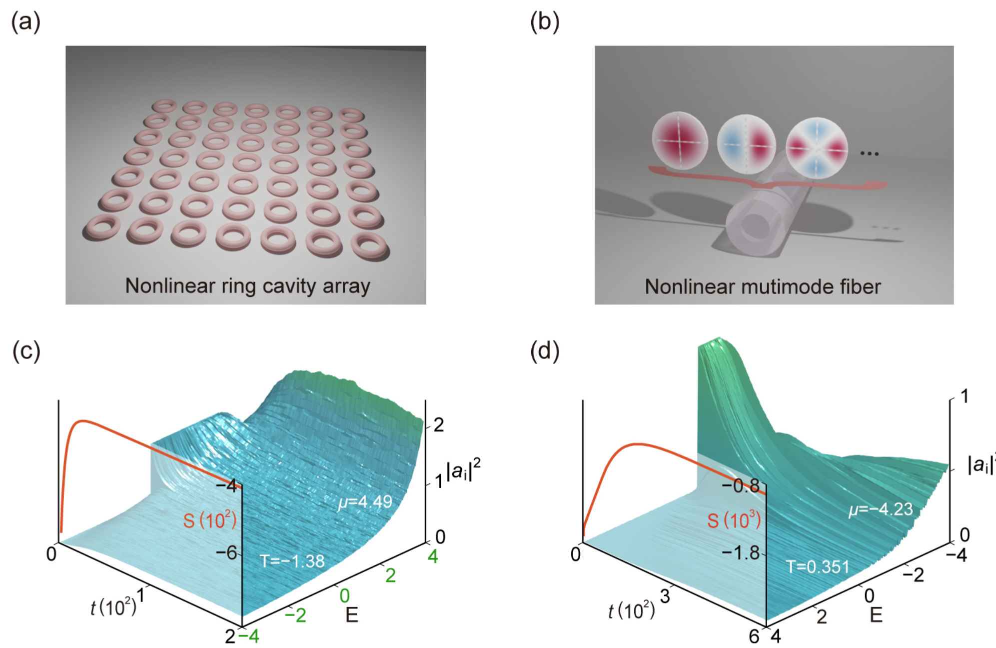

FIG. 1. Emergent photon thermalization in nonlinear multimode optical systems (NLMMOSs). (a) Schematic of a coupled ring cavity array with nonlinear effects. (b) Schematic of a nonlinear multimode fiber supporting many propagating modes. (c) and (d) Thermalization as revealed by the evolution of the mode occupancy $|a_i|^2$ in a coupled ring cavity array with different initial conditions. We use a simple square lattice array with 20×20 sites of the same on-site energy. The equilibrium distribution follows the Rayleigh-Jeans form, showing negative and positive temperatures in (c) and (d), separately. The reversed energy axes are labeled by different colors. Red curves in semitransparent panels give the increasing optical entropy ($S = \sum_{i=1}^{M} \ln|a_i|^2$) as a function of time.

latter different. First, NLMMOSs have remarkable tunability in the couplings between the modes at different sites. Such couplings can be tuned almost at will. Second, the input distribution of photons can be tailored freely. Furthermore, the experimental measurement of photon distribution, fluctuation, and correlation are straightforward and available within current technology. Finally, we remark that photon loss can be a problem for the study of thermodynamics and statistical physics in NLMMOSs, if the lifetime of photons is not long enough. In experiments, high-quality photonic modes have been realized in various optical systems [66–68].

According to Ref. [41], the thermodynamic behaviors of the photonic system in NLMMOSs can be described by introducing several thermodynamic quantities. First, the optical power P is defined as the sum of the mode occupancy coefficient ($a_i = \langle\psi_i|\psi\rangle$) as given by $P = \sum_i^M |a_i|^2$. We use the analog of quantum states and the Dirac notation to formulate the theory, as the system is essentially described by a nonlinear Schrödinger equation. Here, i denotes the mode index, ψ_i is the ith eigenstate of the photonic system without the nonlinear effect, M is the total number of such eigenstates, and $|\psi\rangle$ stands for the photonic state of the entire system. Therefore, P can be regarded as related to the total photon numbers which are preserved in the absence of gain and loss if we consider Kerr nonlinearity. Another invariant is the total energy of the photonic system as represented by the Hamiltonian which can be divided into the linear and nonlinear parts $H = H_{\mathrm{L}} + H_{\mathrm{NL}}$. The weight of the nonlinear Hamiltonian H_{NL} depends on the optical power and the strength of the nonlinear coefficients. Under the weak nonlinearity assumption, the system Hamiltonian is dominated by its linear part $H \approx H_{\mathrm{L}}$. Therefore, the internal energy U can be defined as $U = \sum_i^M \varepsilon_i|a_i|^2$, where ε_i is the eigenenergy of the ith eigenstate. Here, it is worth remarking that, throughout this paper, we adopt the notation specific to coupled optical cavity systems that evolve over time. In contrast, for multimode optical fibers, the definition of energy usually involves a minus sign since, there, the fundamental mode often has the largest quasienergy eigenvalue. Apart from such a difference, the framework of the theory is very much the same for coupled cavity systems and multimode optical fibers. For a detailed comparison of notations, please refer to Ref. [41].

The nonlinear effect here is crucial for the energy exchange among the different eigenmodes. Such energy exchange drives the system to ergodically go through all the microstates on constant power and energy manifolds in a fair manner, like in microcanonical thermodynamic ensembles. This aspect has been numerically verified for various lattice types, dimensions, and nonlinear effects and is universal behavior in NLMMOSs when the nonlinearity is not too strong. Since photons are bosons and the number of photons is much greater than the number of modes, maximization of entropy leads to a special case of Bose-Einstein distribution—Rayleigh-Jeans distribution. In this case, the Gibbs entropy S of the system can be written as $S = M + \sum_{i=1}^M \ln|a_i|^2$ (see Note A in the Supplemental Material [69] for the derivation; in this paper, we set $k_B = 1$) [43]. At thermodynamic equilibrium, the mode occupancy coefficient at thermodynamic equilibrium state is found as [43]

$$|a_i|^2 = \frac{T}{\varepsilon_i - \mu}. \tag{1}$$

Reversely, the temperature and chemical potential can be determined from a steady-state photon distribution $|a_i|$ (see Note B in the Supplemental Material [69] for more details). The above Rayleigh-Jeans distribution implies emergent thermodynamics and statistical physics with the effective temperature and chemical potential. As shown below, the effective temperature can even be negative. While in classical black-body radiation the photonic chemical potential is always vanishing, the photon chemical potential here is often nonzero, as constrained by the total photon number.

To directly visualize the above thermalization process, we calculate the evolution of the mode occupancy coefficient with different initial conditions. The model system is a uniform square lattice with 20×20 sites, and the coupling κ between the nearest sites is set as unit 1. The corresponding Hamiltonian operator takes the following form:

$$\hat{H} = -\sum_{\langle m,n\rangle} \kappa \hat{c}_m^\dagger \hat{c}_n - \frac{1}{2}\sum_m \chi^{(3)} \hat{c}_m^\dagger \hat{c}_m \hat{c}_m^\dagger \hat{c}_m, \tag{2}$$

where $\langle m, n\rangle$ denotes the nearest-neighboring sites. That is, the linear part of the Hamiltonian is determined by the nearest-neighbor couplings, while the nonlinear part is governed by, e.g., the Kerr nonlinearity. The equation of motion is given by the nonlinear Schrödinger equation (see Note C in the Supplemental Material [69] for the procedure toward dimensionless quantities):

$$i\frac{d\psi_m}{dt} + \sum_{\langle m,n\rangle} \kappa a_n + \chi^{(3)}|\psi_m|^2\psi_m = 0. \tag{3}$$

Here, $\psi_{m/n}$, which is the expectation value $\langle \hat{c}_{m/n}\rangle$ of the annihilation operator $\hat{c}_{m/n}$, acts as the time-dependent wave function at the site m/n of the NLMMOS. This mean-field equation holds when the photon occupation number of each mode is very large, which is often the case for most optical systems. In this regime, by replacing operators with their expectations, the Heisenberg equation of motion for the annihilation operators can be transformed into the nonlinear Schrödinger equation for waves to capture the collective behavior of photons. Note that, for simplicity, the above equations are all written in a dimensionless manner. Based on Eq. (3), one can simulate the thermalization process with various initial conditions. As shown in Figs. 1(c) and 1(d), the photonic system reaches the thermal equilibrium state after a short period of time, directly visualizing the thermalization process. During such processes, the entropy of the system increases monotonically until it reaches its equilibrium state.

It is worth mentioning that, to simulate the dynamics of a microcanonical ensemble, we numerically integrated the above nonlinear Schrödinger equation numerically 8000 times with the same initial mode distribution $|a_i|^2$ but with the random initial phase ϕ_i [i.e., $a_i \rightarrow a_i \exp(i\phi_i)$] that is uniformly distributed in [0, 2π]. Such numerical calculations provide a random ensemble to mimic the long-time average of the dynamics in a microcanonical ensemble [42]. Throughout this paper, all observables are calculated via such ensemble averages.

It can be found from Figs. 1(c) and 1(d) that the equilibrium temperature and chemical potential can be well controlled by the initial condition. In Fig. 1(c), we choose the initial distribution as a rectangular distribution with $|a_i|^2 = 1$ for a finite energy region [0, 3]. After the thermalization process (with a time scale $\sim$40), the system reaches an equilibrium state with $T = -1.38$ and $\mu = 4.49$. If the initial distribution is set as $|a_i|^2 = 1$ for the energy region [−2, −1] as in Fig. 1(d), then the equilibrium state has $T = 0.351$ and $\mu = -4.23$ (see Note B in the Supplemental Material [69] for more details). For these two cases, the conserved internal energy and optical power are $U = 212.10$ and $P = 170$ for Fig. 1(c) [$U = -75.64$ and $P = 51$ for Fig. 1(d)]. Figures 1(c) and 1(d) also show that, in the thermalization process, the entropy of the system increases continuously before finally reaching the thermal equilibrium state which is featured by constant entropy and Rayleigh-Jeans distribution.

An intriguing property of the thermodynamics in NLMMOSs is that these systems can exhibit negative temperatures. In fact, negative temperature can be obtained by continuously tuning the parameter $\beta = 1/T$ from positive to negative across zero (meanwhile, the temperature goes from positive infinite to negative infinite). Since the systems studied here have cutoffs in both the high and low frequencies, there is no catastrophe in Rayleigh-Jeans distribution for both positive and negative temperatures. It is worth mentioning that, in previous experiments in systems with energy or frequency cutoffs, negative temperatures have been confirmed [70,71]. Finally, the thermal equilibrium states in NLMMOS can be characterized by the following equation of state [41]:

$$U - \mu P = MT, \tag{4}$$

which is analogous to the state equation of ideal gas. This equation determines the two intensive quantities T and μ through the three extensive quantities M, U, and P. Here, it is assumed that the system is completely isolated from the environment. It is required that the photon lifetime is long enough, which is typically satisfied when the quality factors of the cavities (or waveguides) are $\gtrsim 10^4$—a criterion that can be met in many photonic systems.

III. FCS THEORY

In this paper, we study the nonequilibrium steady-state transport [72–74] between optical systems, through the method based on the joint particle and energy FCS [75–79]. The core of this theory is to obtain the cumulant generating function (CGF) [80] which contains the full information of the transport current and their fluctuations. To rationalize the derivation process, we need to introduce a two-point measurement scheme.

Consider an observable $\hat{B}(t)$ in the Schrödinger picture, where the time variation of operators only stems from external driving. The observable $\hat{B}(t)$ will be either an energy operator $\hat{H}$ or a particle number operator $\hat{N}$. The eigenvalues (eigenvectors) of $\hat{B}(t)$ are labeled by b_t ($|b_t\rangle$) and $\hat{B}(t) = \sum |b_t\rangle b_t \langle b_t|$. The two-point measurement scheme contains the measurement with outcome b_0 at time $t = 0$ and the measurement with outcome b_t at time t as described by the joint probability

$$P[b_t, b_0] \equiv \mathrm{Tr}\{\hat{P}_{b_t}\hat{U}(t,0)\hat{P}_{b_0}\hat{\rho}_0\hat{P}_{b_0}\hat{U}^\dagger(t,0)\hat{P}_{b_t}\} = P^*[b_t, b_0], \tag{5}$$

where $\hat{U}(t,0)$ is the time evolution operator, $\hat{\rho}_0$ denotes the initial density matrix, and the density matrix after time evolution is $\hat{\rho}(t)=\hat{U}(t,0)\hat{\rho}_0\hat{U}^\dagger(t,0)$. The projection operator is $\hat{P}_{b_t}=|b_t\rangle\langle b_t|$, which satisfies the relations $\hat{P}_{b_t}=\hat{P}^2_{b_t}$ and $\sum_{b_t}\hat{P}_{b_t}=\hat{1}$. It is easy to find the normalization of the probabilities $\sum_{b_0,b_t}P[b_t,b_0]=1$.

The probability for the difference $\Delta b=b_t-b_0$ between the two measured outcomes is

$$p(\Delta b)=\sum_{b_t,b_0}\delta(\Delta b-b_t+b_0)P[b_t,b_0]. \tag{6}$$

The generating function (GF) for such a probability is

$$\begin{aligned}G(\lambda)&\equiv\int_{-\infty}^{\infty}d\Delta b\exp(i\lambda\Delta b)p(\Delta b)=G^*(-\lambda)\\&=\sum_{b_t,b_0}\exp[i\lambda(b_t-b_0)]P[b_t,b_0].\end{aligned}\tag{7}$$

Here, λ is the counting field conjugated to the random variable Δb. By substituting Eq. (5) into Eq. (7), the GF has another expression:

$$G(\lambda)=\mathrm{Tr}\hat{\rho}(\lambda,t). \tag{8}$$

where $\hat{\rho}(\lambda,t)\equiv\hat{U}_{\lambda/2}(t,0)\hat{\rho}_0\hat{U}^\dagger_{-\lambda/2}(t,0)$ and $\hat{U}_\lambda(t,0)\equiv\exp[i\lambda\hat{B}(t)]\hat{U}(t,0)\exp[-i\lambda\hat{B}(0)]$. For $\lambda=0$, $\hat{\rho}(\lambda,t)$ reduces to the density matrix of the system $\hat{\rho}(t)$, and $\hat{U}_\lambda(t,0)$ reduces to the standard time evolution operator $\hat{U}(t,0)$.

Taking the logarithm of the GF, we get the expression for the cumulant GF (CGF)

$$\mathcal{Z}(\lambda)=\ln G(\lambda), \tag{9}$$

whose nth derivative with respect to λ evaluated at $\lambda=0$ gives the nth cumulant K_n of $p(\Delta b)$

$$K_n=(-i)^n\frac{\partial^n}{\partial\lambda^n}\mathcal{Z}(\lambda)\Big|_{\lambda=0}. \tag{10}$$

For instance, the first cumulant K_1 gives the average of Δb, $K_1=\langle\Delta b\rangle$ which characterizes the energy or particle number change in a thermodynamic system in the time duration t. This quantity is then connected to the energy or particle current flowing into the system of concern, i.e.,

$$I=\frac{K_1}{t}, \tag{11}$$

in the long-time limit. Here, $K_2=\langle\Delta b^2\rangle-\langle\Delta b\rangle^2$ gives the variance of Δb, and $K_3=\langle(\Delta b-\langle\Delta b\rangle)^3\rangle$ gives the skewness of Δb. These and the other higher cumulants give the fluctuations of the energy and particle currents.

At nonequilibrium steady states, the cumulants vary linearly with time. Therefore, it is natural to define the long-time limit of the CGF

$$S(\lambda)=\lim_{t\to\infty}\frac{1}{t}\mathcal{Z}(\lambda). \tag{12}$$

Like the CGF, taking derivation on the long-time limit of CGF can directly obtain the long-time average of the above cumulants and give direct information about the transport energy and particle currents as well as their fluctuations.

IV. OPTICAL THERMOELECTRIC TRANSPORT

In electronic systems with temperature or chemical potential bias, electrons above and below the chemical potential flow according to these biases, leading to net heat and charge currents. This phenomenon is called the *thermoelectric effect* [81–84]. Similarly, for the transport between two connected NLMMOSs, there can be particle and heat currents, which is a feature distinct from the conventional black-body thermal radiation. This feature emerges because the photonic distributions here are characterized by the temperature and the chemical potential—both are tunable. The particle and heat currents should be considered independently in generic transport setups. We term such transport with both particle and heat currents as optical thermoelectric transport and the related effects as optical thermoelectric effects.

A prototype of such transport systems is based on two infinite photonic reservoirs maintained at different temperatures and chemical potentials, contacting via an embedded small system, as illustrated in Fig. 2(a) (called the two-reservoir setup). The Hamiltonian of the whole system reads $\hat{H}=\hat{H}_{\mathrm{Res}}+\hat{H}_S+\hat{V}$, where $\hat{H}_{\mathrm{Res}}=\hat{H}_L+\hat{H}_R$ represents the Hamiltonian of the two photonic reservoirs (L and R), $\hat{H}_S$ gives the Hamiltonian of the embedded small system, and $\hat{V}$ stands for the interactions among them.

For the total system without external driving, the observable $\hat{B}(t)$ is time independent. The dynamics of the modified time evolution operator satisfies

$$\frac{d}{dt}\hat{U}_\lambda(t,0)=-i\hat{H}_\lambda(t)\hat{U}_\lambda(t,0), \tag{13}$$

where $\hat{H}_\lambda(t)$ is the modified Hamiltonian defined as

$$\hat{H}_\lambda(t)\equiv\exp[i\lambda\hat{B}(t)]\hat{H}(t)\exp[-i\lambda\hat{B}(t)]. \tag{14}$$

Further on, the modified evolution operator can be expressed as

$$\begin{aligned}\hat{U}_\lambda(t,0)&=\exp_+\left\{-i\int_0^t d\tau\hat{H}_\lambda(\tau)\right\}\\ \hat{U}^\dagger_{-\lambda}(t,0)&=\exp_-\left\{i\int_0^t d\tau\hat{H}_{-\lambda}(\tau)\right\},\end{aligned}\tag{15}$$

where the subscripts on the exponents represent different contour-ordering of operators. Given that all the operators mentioned above are in fact time independent, the density matrix can be simplified as

$$\hat{\rho}(\lambda,t)\equiv\exp(-i\hat{H}_\lambda t)\hat{\rho}_0\exp(i\hat{H}_{-\lambda}t). \tag{16}$$

Here, the observables are chosen as the particle number and energy of the left reservoir, and the modified Hamiltonian takes the following form:

$$\begin{aligned}\hat{H}_\lambda&=\exp\left[\frac{i}{2}(\lambda_e\hat{H}_L+\lambda_p\hat{N}_L)\right]\hat{H}\exp\left[-\frac{i}{2}(\lambda_e\hat{H}_L+\lambda_p\hat{N}_L)\right]\\&=\hat{H}_0+\hat{V}_\lambda.\end{aligned}\tag{17}$$

Here, $\hat{H}_0=\hat{H}_{\mathrm{Res}}+\hat{H}_S$ is the λ independent Hamiltonian, and $\hat{V}_\lambda$ is the modified interaction.

The initial state of the total system is considered as a product state $\rho(0)=\rho_L(0)\otimes\rho_R(0)\otimes\rho_S(0)$. As a result, Eq. (8) can be rewritten in terms of the reduced density matrix of the

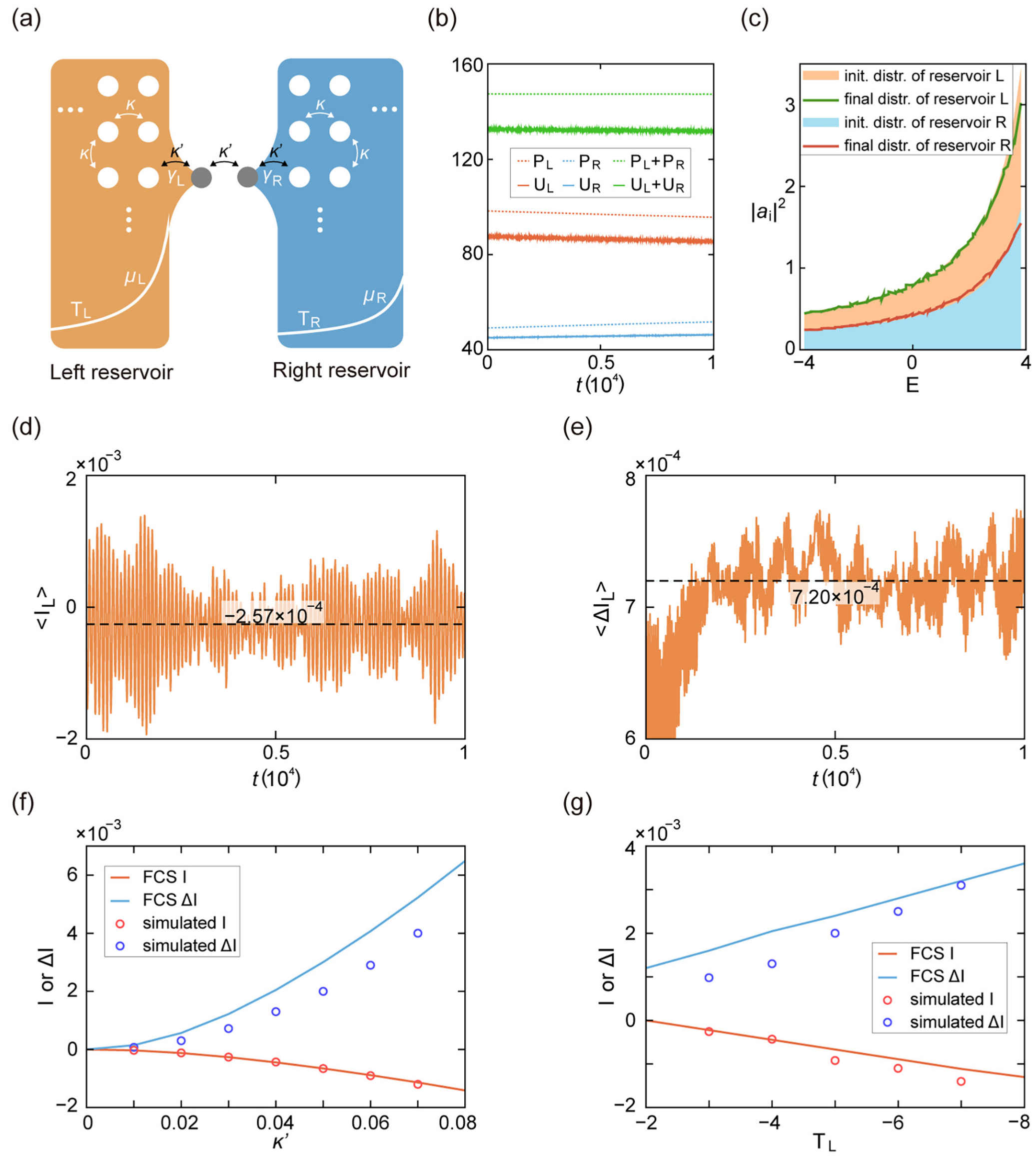

FIG. 2. Transport and fluctuations between two photonic reservoirs. (a) Schematic illustration of the system. Orange and blue regions stand for the left and right reservoirs, respectively. White dots in these regions represent the cavities in the square-lattice nonlinear optical systems that form the two reservoirs. The nearest neighbor coupling between two cavities is κ. A small system with two cavities (gray dots) serves as the bridge between the two reservoirs. The couplings between the two sites of the small system and every two nearest sites of the individual reservoirs are set as κ'. γ_L and γ_R represent the hopping rates of photons transferred from the left and right reservoirs to the small system. (b) Evolution of the optical power P and the internal energy U with time. (c) Initial and final distributions of the two reservoirs from the simulation. (d) Photon current after averaging over 3000 simulations (orange curves) and its long-time averaged value (black dashed line). (e) Variance of the photon current (orange curve) and its long-time averaged value (black dashed line). In (b)–(e), $\kappa' = 0.03$. (f) Dependence of the averaged photon current on the coupling κ'. (g) Long-time averages and variances of photon currents changing with T_L when $\kappa' = 0.04$. Red and cyan curves represent the results from full counting statistics (FCS) theory. Red and blue circles denote the results from the simulations based on the nonlinear Schrödinger equation. The parameters for the two reservoirs are $T_L = -4$, $\mu_L = 5$, $T_R = -2$, and $\mu_R = 5$, unless otherwise specified.

system

$$G(\lambda) = \mathrm{Tr}_S \mathrm{Tr}_{\mathrm{Res}}[\hat{\rho}(\lambda, t)] = \mathrm{Tr}_S \hat{\rho}_S(\lambda, t). \tag{18}$$

We can directly obtain the GF by tracing the density matrix of the small system.

Further on, we try to derive the explicit expression of quantum master equation for photon transport based on the energy level presentation. The total system we considered is composed of two photonic reservoirs connected through a two-level system. Notice that the two reservoirs are decoupled, and the only way to transfer photons is using the two-level system. The eigenstates of reservoirs and system are labeled by i and s, respectively. The Hamiltonian of the whole transport system is $\hat{H} = \hat{H}_L + \hat{H}_R + \hat{H}_S + \hat{V}$:

$$\hat{H}_X = \sum_{i \in X = L,R} \epsilon_i \hat{c}_i^\dagger \hat{c}_i \; \hat{H}_S = \sum_{s \in S} \epsilon_s \hat{c}_s^\dagger \hat{c}_s, \tag{19}$$

where $\hat{c}^\dagger$ and $\hat{c}$ are the photon creation and annihilation operators, which obey the bosonic commutation relations $[\hat{c}_i,\ \hat{c}_j^\dagger] =$

δ_{ij}. The interaction between the reservoir and the small system in the center is described by the hopping between the states s and i:

$$\hat{V}_X = \hat{J}_X^\dagger + \hat{J}_X,\ \hat{J}_X = \sum_{s\in S, i\in X=L,R} J_s^X \hat{c}_s^\dagger \hat{c}_i, \tag{20}$$

where J_s^X represents the couplings between the reservoir and the eigenmode s of the central small system. In this paper, we study the counting statistics of the energy and particles in the left reservoir, which are represented by the Hamiltonian operator and particle number operator, respectively. Therefore, the modified interaction $\hat{V}_\lambda$ in Eq. (17) takes the following form:

$$\begin{aligned}\hat{V}_\lambda &= \exp\left[\frac{i}{2}(\lambda_p\hat{N}_L + \lambda_e\hat{H}_L)\right](\hat{J}_L + \hat{J}_L^\dagger)\\ &\quad\times\exp\left[-\frac{i}{2}(\lambda_p\hat{N}_L + \lambda_e\hat{H}_L)\right] + \hat{V}_R\\ &= \hat{J}_L(\lambda) + \hat{J}_L^\dagger(\lambda) + \hat{V}_R.\end{aligned} \tag{21}$$

Using the fact that, for a boson, $\hat{c}_i\hat{H}_L = (\epsilon_i + \hat{H}_L)\hat{c}_i$, $\hat{J}_L(\lambda)$ in Eq. (21) can be expressed as

$$\hat{J}_L(\lambda) = \sum_{s\in S, i\in L} J_s^L \hat{c}_s^\dagger \hat{c}_i \exp\left(\frac{i}{2}\lambda_p + \frac{i}{2}\lambda_e\epsilon_i\right).$$

Further on, we can define two rates corresponding to the up and down jumping between the eigenstates of the small system via the Born approximation

$$\begin{aligned}k_u^X &= 2\pi g_X(\epsilon_s)\left|J_s^X\right|^2[1 + n_X(\epsilon_s)],\\ k_d^X &= 2\pi g_X(\epsilon_s)\left|J_s^X\right|^2 n_X(\epsilon_s),\\ k_u &= k_u^L + k_u^R,\ k_d = k_d^L + k_d^R.\end{aligned}$$

Here, $g_X(\epsilon_s)$ and $n_X(\epsilon_s)$ are the density of states and the equilibrium distribution of the photonic reservoir $X(= L, R)$ at the energy ϵ_s, respectively. We remark that perturbation theory has been used in the above equations, which implies that the couplings between the small system and the reservoirs are small. In our calculations, we restrict our discussions to the regime with such couplings no larger than 0.1. With these notations, the dynamics of the density matrix of the small system can be expressed as (see details of the derivation in Note D in the Supplemental Material [69])

$$\begin{aligned}&\dot{\hat{\rho}}_S(\lambda, t)\\ &\quad= -i[\hat{H}_S, \hat{\rho}_S(\lambda, t)] + \sum_s -k_u\hat{c}_s^\dagger\hat{c}_s\hat{\rho}_S(\lambda, t) - k_d\hat{c}_s\hat{c}_s^\dagger\hat{\rho}_S(\lambda, t)\\ &\qquad+ \left[k_d^L\exp(i\lambda_p + i\lambda_e\epsilon_i) + k_d^R\right]\hat{c}_s^\dagger\hat{\rho}_S(\lambda, t)\hat{c}_s\\ &\qquad+ \left[k_u^L\exp(-i\lambda_p - i\lambda_e\epsilon_i) + k_u^R\right]\hat{c}_s\hat{\rho}_S(\lambda, t)\hat{c}_s^\dagger.\end{aligned} \tag{22}$$

Throughout this paper, the dot above a symbol stands for the time derivative. In the eigenstate basis of the small system $\{\sum_s |n_s\rangle\}$, Eq. (22) describes the population dynamics of the small system, and

$$\begin{aligned}\dot{\rho}_{n_s}(\lambda, t) &= \sum_s -k_u n_s\rho_{n_s}(\lambda, t) - k_d(1 + n_s)\rho_{n_s}(\lambda, t)\\ &\quad+ \left[k_d^L\exp(i\lambda_p + i\lambda_e\epsilon_i) + k_d^R\right]n_s\rho_{n_s-1}(\lambda, t)\\ &\quad+ \left[k_u^L\exp(-i\lambda_p - i\lambda_e\epsilon_i) + k_u^R\right](n_s + 1)\rho_{n_s+1}(\lambda, t).\end{aligned} \tag{23}$$

Here, $\dot{\rho}_{n_s}(\lambda, t) \equiv \langle n_s|\dot{\hat{\rho}}_S(\lambda, t)|n_s\rangle$, and the subscript s labels the two eigenstates 1 and 2 of the small system [see Fig. 2(a)]. The states of the two-level bosonic system can be denoted as $|n_1, n_2\rangle$, with $n_1, n_2 = 0, 1, 2, \ldots$. The adjacent states $|n_1 \pm 1, n_2\rangle$ and $|n_1, n_2 \pm 1\rangle$, can be connected with $|n_1, n_2\rangle$ by transferring a photon between the small system and the reservoirs. The population dynamics in Eq. (23) can, in fact, be separated into two decoupled parts which can be cast into the matrix form $\dot{\rho}_{n_s} = M_s\rho_{n_s}$, with $s = (1,\ 2)$.

Unlike fermions obeying the Pauli exclusion principle, the number of photons at an eigenmode is unrestricted. In fact, the matrix M_s is infinitely large and tridiagonal

$$M_s = \begin{pmatrix} O_2 & U & 0 & 0 & 0 & 0 & \cdots\\ D & O_1 + 2O_2 & 2U & 0 & 0 & 0 & \cdots\\ 0 & 2D & 2O_1 + 3O_2 & 3U & 0 & 0 & \cdots\\ 0 & 0 & 3D & 3O_1 + 4O_2 & 4U & 0 & \cdots\\ 0 & 0 & 0 & 4D & 4O_1 + 5O_2 & 5U & \cdots\\ 0 & 0 & 0 & 0 & 5D & 5O_1 + 6O_2 & \cdots\\ \vdots & \vdots & \vdots & \vdots & \vdots & \vdots & \ddots \end{pmatrix}. \tag{24}$$

Here,

$$\begin{aligned}O_1 &= -k_d^L - k_d^R, \quad O_2 = -k_u^L - k_u^R,\\ D &= \exp(i\lambda_p + i\lambda_e\epsilon_i)k_d^L + k_d^R,\\ U &= \exp(-i\lambda_p - i\lambda_e\epsilon_i)k_u^L + k_u^R.\end{aligned} \tag{25}$$

The long-time limit behavior of the CGF is dominated by the largest negative eigenvalues of M_s:

$$S(\lambda) = \lim_{t\to\infty}\frac{1}{t}\ln G(\lambda, t) = \sum_{s=1,2} v_{\max}^s. \tag{26}$$

Here, $v_{\max}^s$ is the largest negative eigenvalues of M_s with $s = (1,\ 2)$. By numerically calculating $S(\lambda)$ based on Eqs. (24)–(26) and taking the derivative of $S(\lambda)$ with respect to λ at $\lambda = 0$, as Eq. (10) states, we can obtain the long-time averaged transport currents and their fluctuations, as is done in the following sections. It is worth mentioning that truncating M_s into a 12×12 finite matrix is often sufficient to converge the numerical calculations of the currents and their variances in the parameter regime we studied (see Note E in the Supplemental Material [69] for details). Additionally, we remark that our results are consistent with the second-order perturbation theory based on the Landauer formula at the same order of the small system–reservoir couplings, both yielding the following results:

$$\langle I\rangle = \sum_s \frac{\gamma_s^L\gamma_s^R}{\gamma_s^L+\gamma_s^R}\times[n_L(\epsilon_s)-n_R(\epsilon_s)], \tag{27A}$$

$$\langle I_E\rangle = \sum_s \epsilon_s\frac{\gamma_s^L\gamma_s^R}{\gamma_s^L+\gamma_s^R}\times[n_L(\epsilon_s)-n_R(\epsilon_s)], \tag{27B}$$

where $\gamma_s^X = 2\pi g_X(\epsilon_s)|J_s^X|^2$, with $X=(L,R)$, is the transition rate for photons at the eigenmode s of the small system to decay into the reservoir X. Here, $n_{L/R}$ represents the photon distribution in the left (right) reservoir which takes the Rayleigh-Jeans distribution [Eq. (1)] of quasiequilibrium states.

V. PHOTON TRANSPORT BETWEEN TWO RESERVOIRS

A. Model setup

When the size is considerably large, a NLMMOS can serve as a photon reservoir owing to its tunable thermodynamic properties that completely depend on the initial conditions. To consider the transport effects, we use two large NLMMOSs as the left and right photonic reservoirs. In our system, each reservoir is a square lattice with 10×10 sites (i.e., mode number $M=100$) with the hopping $\kappa=1$ (i.e., energy spectral range $\Delta E\in[-4,4]$) and the Kerr nonlinearity $\chi^{(3)}=\frac{1}{2}$. Therefore, the entire system has two photonic reservoirs and a small system consisting of two sites that bridge the two photonic reservoirs. The Hamiltonian of the whole system is $\hat{H}=\hat{H}_L+\hat{H}_R+\hat{H}_S+\hat{V}$, where

$$\hat{H}_{L/R} = \sum_{\langle m,n\rangle\in L/R}\kappa\hat{c}_m^\dagger\hat{c}_n + \sum_{m\in L/R}\chi^{(3)}\hat{c}_m^\dagger\hat{c}_m\hat{c}_m^\dagger\hat{c}_m,$$
$$\hat{H}_S = \kappa'\hat{c}_l^\dagger\hat{c}_r+\kappa'\hat{c}_r^\dagger\hat{c}_l\ \hat{V} = \kappa'\hat{c}_l^\dagger\hat{c}_p+\kappa'\hat{c}_r^\dagger\hat{c}_q+\text{H.c.} \tag{28}$$

Here, the Hamiltonians of the reservoirs $\hat{H}_L$ and $\hat{H}_R$ are the same as in Eq. (2). The central small system consists of two sites (l and r) coupled by κ'. The interaction $\hat{V}$ describes the couplings between the small system and the left/right reservoirs which is set to be no larger than 0.1. Here, p and q denote the site numbers in the left and right square lattices that couple with the l and r sites, respectively.

Like Eqs. (19) and (20), Hamiltonians in Eq. (28) can be written in a diagonal form. For example, the diagonalization of $\hat{H}_S$ is

$$\hat{c}_1 = \frac{\sqrt{2}}{2}\hat{c}_l+\frac{\sqrt{2}}{2}\hat{c}_r \quad \hat{c}_2 = \frac{\sqrt{2}}{2}\hat{c}_l-\frac{\sqrt{2}}{2}\hat{c}_r,$$
$$\epsilon_1=\kappa'\ \epsilon_2=-\kappa',\quad \hat{H}_S=\epsilon_1\hat{c}_1^\dagger\hat{c}_1+\epsilon_2\hat{c}_2^\dagger\hat{c}_2. \tag{29}$$

From the above expressions, the transition rate $\gamma_s^{L(R)}$ can be determined by the Fermi Golden rule

$$\gamma_{1/2}^{L(R)} = \frac{1}{2}\times2\pi|\kappa'|^2 g_{1/2}^{p(q)}$$
$$= \frac{1}{2}\times2\pi|\kappa'|^2\left\{\frac{1}{\pi}\sum_{i\in L(R)}\frac{\Gamma}{(\epsilon_i-\epsilon_{1/2})^2+\Gamma^2}\right\}\left|\psi_{i\in L(R)}^{p(q)}\right|^2. \tag{30}$$

Here, the prepositive $\frac{1}{2}$ stems from the fact that $|\psi_{1/2}^{l(r)}|^2=\frac{1}{2}$, where the superscripts l and r present the two sites of the embedded system, and subscripts 1 and 2 denote the two eigenstates of the small system. Both wave functions $\psi_{1/2}^{l(r)}$ and $\psi_{i\in L(R)}^{p(q)}$ are normalized at the two-point system and square lattice, respectively. Therefore, their moduli squares represent the local density of states at positions l, r, p, and q. The complex term in the $\{\cdots\}$ of Eq. (30) is the Lorentz function that describes the spectral broadening of the states ϵ_1 and ϵ_2 of the small system. The resonance width Γ is set as 0.08 to cover the average level spacing of the left and right reservoirs $\langle\Delta\epsilon\rangle=\Delta E/M$. Thus, the state of the small system $\epsilon_{1/2}$ mainly resonates with the neighbor levels of reservoirs.

In our simulations, to reduce the run time and give more information on the transport processes, the initial distribution in each reservoir is set as the equilibrium Rayleigh-Jeans distribution with a randomized phase (uniformly distributed in the region $[0,\ 2\pi]$) at each eigenstate. Repetitions of the evolution process are set as 3000 times to obtain sufficient data for statistical analysis.

B. Photon transport at negative temperatures

In this section, we present the nonequilibrium steady-state photon transport in our system as characterized by the long-time limit CGF [Eq. (26)] and compare the results from FCS theory with the first-principles simulations based on the nonlinear Schrödinger equation. We are more interested in the regime where at least one of the reservoirs has negative temperatures. The nonequilibrium steady-state photon transport demands that the distributions in the left and right reservoirs are nearly invariant during the transport. Therefore, the coupling κ' connecting the small system to the reservoirs must be set to be very small in the simulations. In addition, the evolution time span in a single simulation is chosen as 10 000 time-units to obtain the long-time behaviors of the nonequilibrium transport. Note that, as we work with the dimensionless nonlinear Schrödinger equation [Eq. (3)], every quantity has a natural unit (e.g., the energy unit is the hopping coupling in the reservoirs, from which the time unit can be determined via the uncertainty relation; when compared with experiments, the energy and time units can be determined rigorously; see Note C in the Supplemental Material [69] for more information).

We now use an example to demonstrate the steady-state transport in our system via the first-principles simulations. As shown in Fig. 2(b), the optical power and internal energy of the left and right photonic reservoirs change very slowly with time. Although this feature is distinct from the steady-state transport between two reservoirs in the thermodynamic limit, the transport here can still be considered approximately as the steady-state transport. There are other interesting features in Fig. 2(b). We find that the total optical power P_L+P_R is strictly conserved, whereas due to the nonlinear interactions, the total internal energy U_L+U_R (as is defined solely on the linear energy) is not a conserved quantity. Nevertheless, the total internal energy U_L+U_R is approximately conserved at long timescales, with fast fluctuations at a short timescale of 8 time-units. Thus, thermodynamics and nonequilibrium steady-state transport theories are still valid at very long timescales.

Figure 2(c) verifies the steady-state transport from the aspect of the distributions in the reservoirs. The initial and final distributions during the entire time interval of 10 000 time-units almost overlap with each other, which indicates that the change of the distributions during the whole transport process is negligible—a notable feature of the steady-state transport.

In this section, we study only the photon particle current and its fluctuations which are well-defined in the simulation and FCS theory. In the simulation, the currents are obtained via the Heisenberg equation of motion $\hat{I}_{L/R} = \frac{d}{dt}\hat{N}_{L/R} = i[\hat{H}, \hat{N}_{L/R}]$, where $\hat{N}_{L/R} = \sum_{m\in L/R} \hat{c}_m^\dagger \hat{c}_m$ is the total particle number in the left/right reservoir. For the left and right reservoirs, we obtain, respectively, the following photon current operators for the left and right systems:

$$\hat{I}_L = i[\kappa'\hat{c}_p^\dagger\hat{c}_l + \kappa'\hat{c}_l^\dagger\hat{c}_p, \hat{c}_p^\dagger\hat{c}_p] = i\kappa'(\hat{c}_l^\dagger\hat{c}_p - \hat{c}_p^\dagger\hat{c}_l),$$
$$\hat{I}_R = i[\kappa'\hat{c}_q^\dagger\hat{c}_r + \kappa'\hat{c}_r^\dagger\hat{c}_q, \hat{c}_q^\dagger\hat{c}_q] = i\kappa'(\hat{c}_r^\dagger\hat{c}_q - \hat{c}_q^\dagger\hat{c}_r). \quad (31)$$

We extract the instant photon current in each simulation for every 2.5 time-units (totally 10 000 time-units for a single simulation) by taking the expectation value of the above operators using the instant photonic wave function. After 3000 simulations, we obtain an ensemble of 12 million data points of these currents which is sufficiently large to perform statistical analysis. To avoid confusion, we note that, in the following, the symbols $\langle \mathrm{I}\rangle$ and $\langle \Delta\mathrm{I}\rangle = \langle \mathrm{I}^2\rangle - \langle \mathrm{I}\rangle^2$ stand, respectively, for the average and variance of the currents averaged over an ensemble of 3000 repeated simulations with the randomized initial phase condition at a certain time. In contrast, for the currents and their variance averaged over both the ensemble and the long timescale, the average symbol $\langle \ldots \rangle$ is omitted.

The steady-state transport implies $I_L = -I_R$ and $\Delta I_L = \Delta I_R$. Thus, the photon current from the left reservoir to the right reservoir is equal to $I = -I_L = I_R$. We thus only present the results for the photon currents flowing into the left reservoir. In Fig. 2(d), we find that the 3000-simulation-averaged photon current fluctuates around its long-time-averaged value (i.e., the black dashed line). The variance of photon currents ΔI_L shown in Fig. 2(e) is larger than the photon current I_L. Thus, the direction of photon currents may reverse in the transient dynamics. Additionally, fluctuations are significantly more pronounced at the beginning than the rest of the time. This feature indicates that the system reaches steady-state transport at about $t = 3000$. Therefore, we only use the data from $t = 3000$ to 10 000 for the long-time averages.

The photon current and its variance averaged over both the ensemble and the long timescale are labeled by the black dashed lines in Figs. 2(d) and 2(e). These averaged values are $I_L = -2.57 \times 10^{-4}$ and $\Delta I_L = 0.72 \times 10^{-3}$. Surprisingly, FCS theory gives comparable values through Eq. (10): $I_L = -2.65 \times 10^{-4}$ and $\Delta I_L = 1.20 \times 10^{-3}$, although these two approaches are quite different. On the one hand, FCS theory assumes that the reservoirs are in the thermodynamic limit, i.e., infinitely large, and are kept at thermal equilibrium. FCS theory is essentially a stochastic approach based on quantum perturbation theory. On the other hand, the simulation is based solely on the nonlinear Schrödinger equation, which contains purely deterministic dynamics. The consistency between the two approaches suggests that the statistical theory agrees well with the deterministic dynamic theory in our system, which is quite noteworthy. These results indicate that it is possible to compare statistical physics theory and dynamic simulations quantitatively in certain regimes when thermodynamic behaviors can be captured by the first-principles calculations of the deterministic dynamics.

We further examine the photon current and its variance for various system parameters. In Fig. 2(f), we study the dependence of these quantities on the system-reservoir coupling κ'. It is found that the photon current increases with κ' in nearly quadratic form, while the variance of the photon current also increases with κ' in similar form but much more rapidly. The quadratic increase of the photon current is consistent with Eq. (27) since both γ_s^L and γ_s^R are proportional to κ'^2. At large κ', higher-order corrections come into play, and the dependence deviates from $\sim\kappa'^2$. The calculation results from the first-principles simulations and FCS theory are comparable and qualitatively consistent with one another. The photon currents obtained from the two approaches agree excellently with each other. In Fig. 2(g), we investigate the photon current and its variance when only the temperature of the left photonic reservoir T_L changes. As T_L increases, the temperature difference increases, and the photon current ramps up, while the variance of the photon current also increases. At $T_L = -2$, there is no bias in the temperature or chemical potential. The average photon current vanishes. Nevertheless, the variance of the photon current is nonzero—an intrinsic feature of thermodynamic equilibrium.

C. Loop currents between positive- and negative-temperature reservoirs

We now study the intriguing transport between positive- and negative-temperature reservoirs and reveal an interesting phenomenon we have named *loop currents*. We stress that the setup studied here is not available in systems other than photons in NLMMOSs. To be concrete, we set the initial conditions for the left and right reservoirs as $T_L = -2$, $\mu_L = 5$, $T_R = 2$, and $\mu_R = -5$. It is crucial to note that the spectra of the two reservoirs and the small system are symmetric with respect to zero energy (for a specific optical system, the zero energy is defined as the average on-site energy for the cavities). In that case, the distributions in the left and right reservoirs are inverted. Meanwhile, the coupling between the two sites in the small system gives rise to an even-parity eigenstate (antibonding state) with positive energy and an odd-parity eigenstate (bonding state) with negative energy. Tunneling via the even state transfers photons from the left reservoir to the right reservoir in the positive energy channel, whereas the odd state offers a negative energy channel to transfer photons from the right reservoir to the left reservoir. These transferred photons are then thermalized via nonlinear interaction. For instance, high (low)-energy photons in the right (left) reservoir give (take) energy to (from) other photons in the same reservoir via nonlinear interaction. This scenario, as schematically depicted in Fig. 3(a), gives rise to the phenomenon termed as the loop current: In the positive energy sector, photons flow from the left reservoir to the right, while in the negative energy sector, photons flow from the right

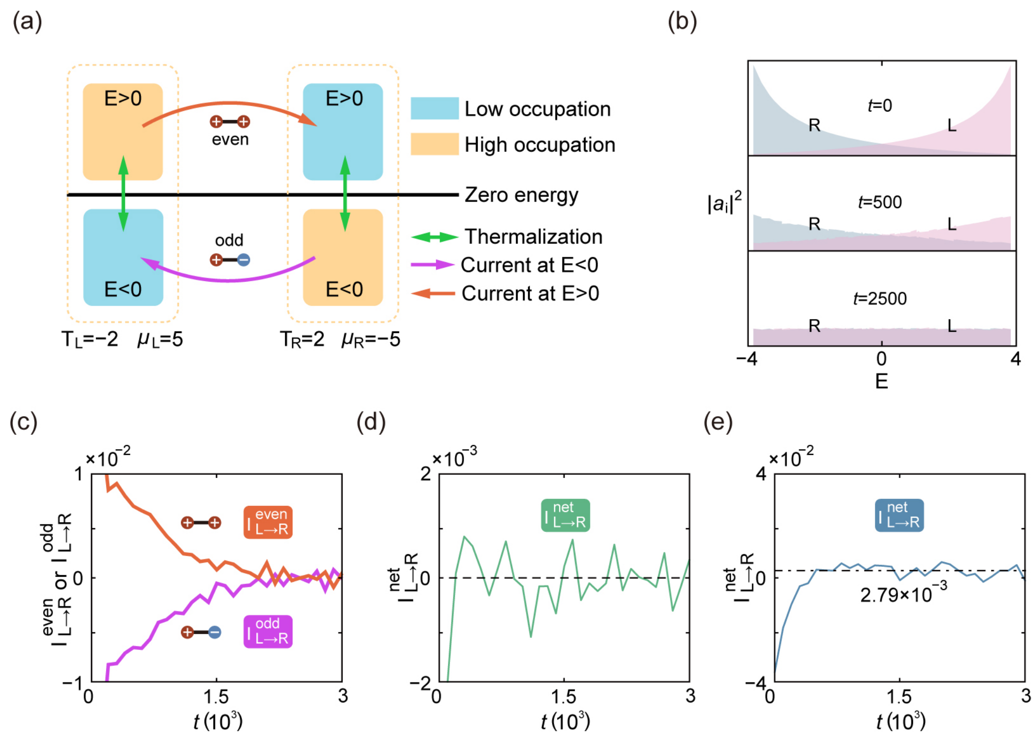

FIG. 3. Transport between two reservoirs with opposite temperatures and chemical potentials. (a) Schematic of the loop current effect when the system has particle-hole symmetry. Red and purple arrows denote the opposite currents in the positive and negative energy sectors via, respectively, the even and odd modes of the small system. Green arrows denote the energy exchange between the positive and negative energy sectors in each reservoir due to thermalization processes via nonlinear interactions. (b) Distributions in the two reservoirs at three different times: $t = 0$, 500, and 2500. (c) Evolution of photon current in the positive and negative energy sectors. Current in the positive (negative) energy sector is through the even (odd) mode of the small system which is denoted by the superscript even (odd). (d) Evolution of the net photon current for the same condition as in (c). The black dashed line indicates the zero current around which the net current fluctuates. (e) Evolution of the net photon current when the on-site energy of the two cavities in the small system is raised from 0 to 1. The number gives the long-time averaged (starting from $t = 1250$) value of the current which is labeled by the black dot-dashed line. The parameters are $\kappa' = 1$, $T_L = -2$, $\mu_L = 5$, $T_R = 2$, and $\mu_R = -5$. For all calculations, the current is averaged in the time interval of 100 time-units. To keep the particle-hole symmetry of the whole system, the sign of the nonlinear coefficient $\chi^{(3)}$ is flipped for adjacent sites in each reservoir, while its amplitude is fixed to $\frac{1}{2}$.

reservoir to the left. In each reservoir, nonlinear interaction enables energy exchange and thermalization [85]. Eventually, the distributions in the two reservoirs become the same, and the whole system reaches thermodynamic equilibrium with infinite temperature [Fig. 3(b)].

In Fig. 3(b), we give the distributions in the two reservoirs at different times $t = 0$, 500, and 2500 from the first-principles simulations (to enlarge the loop current effect, we set $\kappa' = 1$). These snapshots indicate the evolution of the distributions in the reservoirs. Initially, due to the inversed temperatures and chemical potentials, the distributions in the two reservoirs are related to each other by particle-hole symmetry, i.e., mirror symmetric with respect to zero energy. At $t = 500$, this symmetry still holds, indicating that photons with opposite energies are transported at the same rate, which agrees with the scenario illustrated in Fig. 3(a). After a long time, at $t = 2500$, the distributions in the two reservoirs become flat and identical, indicating the equilibrium state of the whole system which has infinite temperature. It is worth noting that the photon distribution in this paper is only proportional to the actual photon numbers (up to a constant determined by the total optical power; see Note C in the Supplemental Material [69] for the relation between the dimensionless quantities and physical quantities). In fact, it is difficult to determine the actual photon number in experiments, while the distribution can be measured easily up to a constant determined by the photon detection probability.

To reveal the loop current effect, we present the evolution of the currents in the positive and negative energy sectors in Fig. 3(c). It is found that these two currents are approximately opposite to each other. By adding these two currents, we find that the net current is fluctuating around zero in Fig. 3(d). In fact, the long-time-averaged net current is close to zero, confirming again the loop current picture in Fig. 3(a). To observe nonzero net photon current, we need to break particle-hole symmetry. This can be done by raising the energy levels of the small system by 1, as in Fig. 3(e). With this change, we find from simulations that a finite net photon current emerges near the initial time. The phenomenon of loop current serves as a compelling illustration of the impact of symmetry on the photon transport. Particularly, the net photon current is nonzero only when the photonic Hamiltonian breaks particle-hole symmetry. This property illustrates the pivotal role of symmetry on nonequilibrium phenomena.

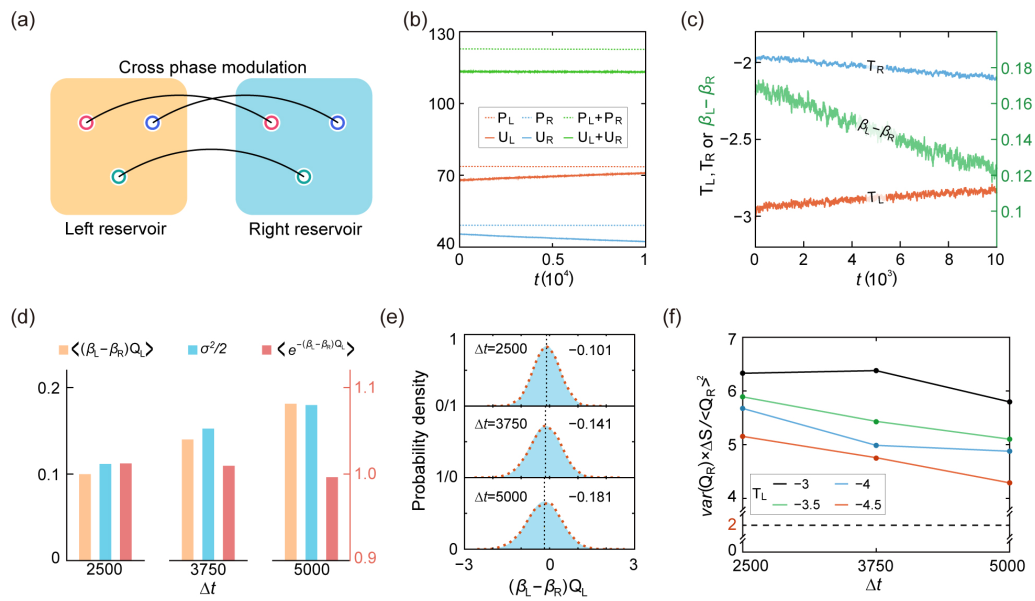

FIG. 4. Heat exchange between negative temperature reservoirs and the fluctuation theorem. (a) Illustration of the system with heat exchange between two reservoirs that are coupled via the cross-phase modulation (XPM) nonlinear interaction (indicated by the three black curves). (b) Evolution of the optical power in the left and right reservoirs P_L and P_R and their summation as well as the internal energy in the left and right reservoirs U_L and U_R and their summation. The total particle number and internal energy are conserved. (c) Evolution of the temperatures of the left and right reservoirs and the difference in the inverse temperature for the two reservoirs $\beta_L - \beta_R$ (its value is given by the right vertical axis). (d) Three quantities $\langle(\beta_L - \beta_R)Q_L\rangle$, $\sigma^2/2$, and $\langle\exp[-(\beta_L - \beta_R)Q_L]\rangle$, measured during different time spans. Here, σ^2 is the variance of $(\beta_L - \beta_R)Q_L$. From left to right, the exact values of the columns are {0.101, 0.113, 1.01}, {0.141, 0.153, 1.01}, and {0.181, 0.180, 1.00} for these three quantities. Note that the value of $\langle(\beta_L - \beta_R)Q_L\rangle$ is given by the vertical axis at the right side. (e) Normalized probability density distributions of $(\beta_L - \beta_R)Q_L$ calculated for different time spans (red dotted lines) which are consistent with the Gaussian distributions (blue-shaded region) determined via the average value and the variance of $(\beta_L - \beta_R)Q_L$. The numbers give the average value $\langle(\beta_L - \beta_R)Q_L\rangle$. (f) Thermodynamic ratio term $\frac{\mathrm{var}(Q_R)}{\langle Q_R\rangle^2}\Delta S_R$ as the function of time spans for different T_L. Black dashed line means the lower bound of thermodynamic uncertainty relation at the given value 2.

VI. HEAT EXCHANGE FLUCTUATION THEOREM AND THERMODYNAMIC UNCERTAINTY RELATION

In stochastic thermodynamics, the fluctuation theorem [86–89] plays a crucial role. Using step-by-step coarse-graining procedures, the fluctuation theorem can be derived from the detailed balance, which arises from microreversibility [90]. The common fluctuation theorems include Jarzynski's equality for work [91–93], the exchange fluctuation theorem for heat and matter [58,59], and the fluctuation theorem for entropy production [94,95].

Authors of previous studies on the fluctuation theorem have primarily focused on the positive temperature regime, whereas authors of only a few works have discussed the negative temperature regime [96]. Here, we try to verify the heat exchange fluctuation theorem at negative temperatures in an NLMMOS. The basic setup of our system is two coupled reservoirs (i.e., two square lattices with 10×10 sites) which are coupled via optical XPM interactions, as illustrated in Fig. 4(a). Unlike in the previous section, here, there is no small system acting as the bridge between the two reservoirs. Instead, the two reservoirs are coupled by several pairs of sites. Within each pair, the two sites, one from each reservoir, are interconnected through XPM. In this case, the XPM allows energy exchange between the two reservoirs but no photon transfer between the two reservoirs. Initially, the left reservoir has Rayleigh-Jeans distribution with $T_L = -3$ and $\mu_L = 5$, while the right reservoir has $T_R = -2$ and $\mu_R = 5$. In the simulation, we randomly establish the XPM coupling on three pairs of sites (both these sites and their connections are randomly chosen). Here, the nonlinear coefficient $\chi^{(3)}$ for the XPM coupling and the Kerr effect are set as $\frac{1}{8}$ and $\frac{1}{4}$, respectively. The XPM coupling is crucial for the energy exchange between the two reservoirs. Therefore, the internal energy in the two reservoirs U_L and U_R evolve with time, whereas the optical powers P_L and P_R do not change with time since there is no photon exchange between the two reservoirs [see Fig. 3(b)]. A practical way is to consider the XPM couplings as happening only at the boundary between the two reservoirs. Nevertheless, the interest here is to reveal the heat exchange fluctuation theorem holds in NLMMOSs. Compared with the XPM couplings at the boundary, the random XPM couplings give a stronger numerical verification of the heat exchange fluctuation theorem.

In our two-reservoir system, the heat exchange fluctuation theorem takes the form

$$\langle\exp[-(\beta_L - \beta_R)Q_L]\rangle = 1, \tag{32}$$

where Q_L stands for the heat change of the left reservoir between two measured times. Here, $\langle\cdots\rangle$ represents the ensemble average, and β_L and β_R (T_L and T_R) evolve with time due to energy exchange and the finite size of the reservoirs, as shown in Fig. 4(c). Since our two-reservoir system is isolated (without external drive) and photon transport is prohibited (without internal work: $W = \mu\Delta P$), according to the first law of thermodynamics $\Delta U = W + Q$, the heat change Q_L can be simply obtained from the internal energy change ΔU_L.

Numerically, we perform the simulation with the same initial condition (but randomized phases on a_i and random XPM pairs) 3000 times. These 3000 simulations are used as an ensemble to study the statistics of the heat exchange. Figure 4(d) presents the three quantities $\langle(\beta_L - \beta_R)Q_L\rangle$, $\sigma^2/2$ [σ^2 means the variance of $(\beta_L - \beta_R)Q_L$], and $\langle\exp[-(\beta_L - \beta_R)Q_L]\rangle$, for different time spans $\Delta t = 2500,\ 3750,$ and 5000 with the same initial time $t = 5000$. The quantity $\beta_L - \beta_R$ is approximated as the average value in the corresponding time span, i.e., $\beta_L - \beta_R = 0.138,\ 0.136,$ and 0.133, separately. In Fig. 4(d), we show the values of $\langle(\beta_L - \beta_R)Q_L\rangle$ and $\sigma^2/2$ for the three time spans and find that these values agree well with each other. In addition, the ensemble average $\langle\exp[-(\beta_L - \beta_R)Q_L]\rangle$ is very close to 1. These results numerically verify Eq. (32). We further give the histogram distributions of $\langle(\beta_L - \beta_R)Q_L\rangle$ from numerical calculations for the three time spans in Fig. 3(e). It is found that these distributions are in excellent agreement with the Gaussian profile in linear response regions. With this numerical evidence, we verify the fluctuation theorem in the negative temperature regime, extending the fluctuation theorem to an unconventional realm.

Recently, a thermodynamic uncertainty relation has been formulated based on classical Markovian steady states, demonstrating the trade-off relation between relative current fluctuation and dissipation. Specifically, the relation bounds the average accumulated current $\langle Q\rangle$, its variance var(Q), and the entropy production ΔS in a nonequilibrium process [97–100]

$$\frac{\mathrm{var}(Q)}{\langle Q\rangle^2}\Delta S \geqslant 2, \tag{33}$$

with $k_B = 1$. To quantify the presence of noise in the nonlinear photonic system, we will further verify whether the thermodynamic uncertainty relationship holds in our system. In the previous heat exchange system, negative-temperature reservoir R produces entropy due to the loss of energy ΔU_R. Based on the same setup, we validate the thermodynamic ratio term on reservoir R: $\frac{\mathrm{var}(Q_R)}{\langle Q_R\rangle^2}\Delta S_R$, as the black line shown in Fig. 4(f), where the lower bound of Eq. (33) is labeled by the black dashed line. Previous researchers have predominately addressed scenarios involving positive-temperature reservoirs, while investigations into negative-temperature reservoirs have been conspicuously absent. As depicted in the Fig. 4(f), it is evident that the thermodynamic uncertainty relation persists under positive-temperature conditions, aligning with previous research outcomes. Remarkably, this relation also holds true under negative-temperature conditions. This underscores that the polarity of the reservoir temperature, whether positive or negative, does not disrupt the thermodynamic uncertainty relation. It is noteworthy that, as the measurement time interval Δt increases, the ratio of thermodynamic uncertainties at different temperatures gradually converges and approaches 2. This convergence is attributed to enhanced measurement accuracy with prolonged measurement time, leading the system toward stability.

VII. CONCLUSIONS AND DISCUSSIONS

Starting from two distinct approaches, i.e., the first-principles simulations of dynamics via the nonlinear Schrödinger equation and FCS theory of photon transport, we reveal the intriguing transport and fluctuation properties of the NLMMOSs whose equilibrium states are described by Rayleigh-Jeans distributions. We explore the steady-state photon transport and its fluctuations between two finite-sized reservoirs. We find that, surprisingly, those two approaches yield quantitatively comparable results, showing a consistent picture between deterministic Schrödinger dynamics and (stochastic) statistical physics in the description of nonequilibrium photon transport. Additionally, as the NLMMOSs have a finite-ranged photon spectrum, the photon distribution can have negative temperatures—a remarkable property of microcanonical ensembles. We further reveal that, under the circumstance of two reservoirs with opposite temperatures and chemical potentials, an intriguing phenomenon termed the loop current effect can emerge where the current in the positive energy sector is opposite to that of the negative energy sector. This effect also reveals the key role of symmetry in nonequilibrium phenomena. Finally, based on the statistics of the heat currents between the two reservoirs obtained from the nonlinear Schrödinger equation and FCS theory approaches, we numerically verify the fluctuation theorem in the negative-temperature regime. In this paper, we reveal that the photonic transport properties and their statistical fluctuations in NLMMOSs contain rich and intriguing phenomena which are yet to be explored in experiments. Experimental investigators of these phenomena can gain insight into fundamental statistical physics and motivate potential applications such as engineering non-Planckian heat and photon transfer in nonlinear optical fibers and coupled optical resonator systems. Finally, we remark that the whole system is treated as conserved in the study (i.e., photon dissipation is not considered), which is a key starting point for thermodynamics. Of course, this cannot be true in real photonic experiments. Nevertheless, if the lifetime of each photon is significantly larger than the thermalization time in the system, which is about 500 time-units, then the physics studied here can hold true for real experimental systems. For instance, we estimate that, if the photon lifetime is longer than 10 000 time-units, the effects studied here can hold true. In addition, our discussions assume that the nonlinear interaction is not strong. If the nonlinear interaction is very strong, then the system will behave differently, e.g., effects such as bistability will emerge. Here, the relatively weaker nonlinear interaction only leads to photon-photon scattering and photon thermalization, which form the foundation of our study.

ACKNOWLEDGMENTS

J.-H.J. is grateful for support from the National Natural Science Foundation of China (Grant No. 12125504) and the Hundred Talents Program of the Chinese Academy of Sciences. J.L. acknowledges the National Natural Science Foundation of China (Grant No. 12305050) and the Natural

Science Foundation of Jiangsu Higher Education Institutions of China (No. 23KJB140017). Z.X. and Y.C. are funded by the National Natural Science Foundation of China (Grant No. 12274161).

[1] A. Picozzi, J. Garnier, T. Hansson, P. Suret, S. Randoux, G. Millot, and D. N. Christodoulides, Optical wave turbulence: Towards a unified nonequilibrium thermodynamic formulation of statistical nonlinear optics, Phys. Rep. **542**, 1 (2014).

[2] L. Pistone, M. Onorato, and S. Chibbaro, Thermalization in the discrete nonlinear Klein-Gordon chain in the wave-turbulence framework, EPL **121**, 44003 (2018).

[3] W. Fu, Y. Zhang, and H. Zhao, Universal scaling of the thermalization time in one-dimensional lattices, Phys. Rev. E **100**, 010101(R) (2019).

[4] S. Feng, W. Fu, Y. Zhang, and H. Zhao, Phonon damping in one-dimensional lattices with asymmetric interactions, Sci. China: Phys. Mech. Astron. **65**, 117006 (2022).

[5] J. Wang, G. Casati, and G. Benenti, Classical physics and blackbody radiation, Phys. Rev. Lett. **128**, 134101 (2022).

[6] N. Berti, K. Baudin, A. Fusaro, G. Millot, A. Picozzi, and J. Garnier, Interplay of thermalization and strong disorder: Wave turbulence theory, numerical simulations, and experiments in multimode optical fibers, Phys. Rev. Lett. **129**, 063901 (2022).

[7] Y. A. Vlasov, M. A. Kaliteevski, and V. V. Nikolaev, Different regimes of light localization in a disordered photonic crystal, Phys. Rev. B **60**, 1555 (1999).

[8] M. M. Sigalas, C. M. Soukoulis, C. T. Chan, R. Biswas, and K. M. Ho, Effect of disorder on photonic band gaps, Phys. Rev. B **59**, 12767 (1999).

[9] J. Lian, J.-X. Fu, L. Gan, and Z.-Y. Li, Robust and disorder-immune magnetically tunable one-way waveguides in a gyromagnetic photonic crystal, Phys. Rev. B **85**, 125108 (2012).

[10] L. Lu, J. D. Joannopoulos, and M. Soljačić, Topological photonics, Nat. Photon. **8**, 821 (2014).

[11] L.-H. Wu and X. Hu, Scheme for achieving a topological photonic crystal by using dielectric material, Phys. Rev. Lett. **114**, 223901 (2015).

[12] S. Barik, H. Miyake, W. DeGottardi, E. Waks, and M. Hafezi, Two-dimensionally confined topological edge states in photonic crystals, New J. Phys. **18**, 113013 (2016).

[13] J.-W. Dong, X.-D. Chen, H. Zhu, Y. Wang, and X. Zhang, Valley photonic crystals for control of spin and topology, Nat. Mater. **16**, 298 (2017).

[14] Y. Yang, Y. F. Xu, T. Xu, H.-X. Wang, J.-H. Jiang, X. Hu, and Z. H. Hang, Visualization of a unidirectional electromagnetic waveguide using topological photonic crystals made of dielectric materials, Phys. Rev. Lett. **120**, 217401 (2018).

[15] Y. Ota, R. Katsumi, K. Watanabe, S. Iwamoto, and Y. Arakawa, Topological photonic crystal nanocavity laser, Commun. Phys. **1**, 86 (2018).

[16] D. Arovas, J. R. Schrieffer, and F. Wilczek, Fractional statistics and the quantum Hall effect, Phys. Rev. Lett. **53**, 722 (1984).

[17] R. Willett, J. P. Eisenstein, H. L. Störmer, D. C. Tsui, A. C. Gossard, and J. H. English, Observation of an even-denominator quantum number in the fractional quantum Hall effect, Phys. Rev. Lett. **59**, 1776 (1987).

[18] Y. Zhang, Y.-W. Tan, H. L. Stormer, and P. Kim, Experimental observation of the quantum Hall effect and Berry's phase in graphene, Nature (London) **438**, 201 (2005).

[19] B. A. Bernevig and S.-C. Zhang, Quantum spin Hall effect, Phys. Rev. Lett. **96**, 106802 (2006).

[20] K. S. Novoselov, Z. Jiang, Y. Zhang, S. V. Morozov, H. L. Stormer, U. Zeitler, J. C. Maan, G. S. Boebinger, P. Kim, and A. K. Geim, Room-temperature quantum Hall effect in graphene, Science **315**, 1379 (2007).

[21] B. Xie, G. Su, H.-F. Wang, F. Liu, L. Hu, S.-Y. Yu, P. Zhan, M.-H. Lu, Z. Wang, and Y.-F. Chen, Higher-order quantum spin Hall effect in a photonic crystal, Nat. Commun. **11**, 3768 (2020).

[22] X. Huang, Y. Lai, Z. H. Hang, H. Zheng, and C. T. Chan, Dirac cones induced by accidental degeneracy in photonic crystals and zero-refractive-index materials, Nat. Mater. **10**, 582 (2011).

[23] L. Lu, L. Fu, J. D. Joannopoulos, and M. Soljačić, Weyl points and line nodes in gyroid photonic crystals, Nat. Photonics **7**, 294 (2013).

[24] W. Gao, B. Yang, M. Lawrence, F. Fang, B. Béri, and S. Zhang, Photonic Weyl degeneracies in magnetized plasma, Nat. Commun. **7**, 12435 (2016).

[25] G.-G. Liu, P. Zhou, Y. Yang, H. Xue, X. Ren, X. Lin, H.-x. Sun, L. Bi, Y. Chong, and B. Zhang, Observation of an unpaired photonic Dirac point, Nat. Commun. **11**, 1873 (2020).

[26] X. Xi, B. Yan, L. Yang, Y. Meng, Z.-X. Zhu, J.-M. Chen, Z. Wang, P. Zhou, P. P. Shum, Y. Yang *et al.*, Topological antichiral surface states in a magnetic Weyl photonic crystal, Nat. Commun. **14**, 1991 (2023).

[27] L. Feng, R. El-Ganainy, and L. Ge, Non-Hermitian photonics based on parity-time symmetry, Nat. Photon. **11**, 752 (2017).

[28] M. G. Silveirinha, Topological theory of non-Hermitian photonic systems, Phys. Rev. B **99**, 125155 (2019).

[29] X. Zhu, H. Wang, S. K. Gupta, H. Zhang, B. Xie, M. Lu, and Y. Chen, Photonic non-Hermitian skin effect and non-Bloch bulk-boundary correspondence, Phys. Rev. Res. **2**, 013280 (2020).

[30] S. Longhi, Modulational instability and space time dynamics in nonlinear parabolic-index optical fibers, Opt. Lett. **28**, 2363 (2003).

[31] K. Krupa, A. Tonello, A. Barthélémy, V. Couderc, B. M. Shalaby, A. Bendahmane, G. Millot, and S. Wabnitz, Observation of geometric parametric instability induced by the periodic spatial self-imaging of multimode waves, Phys. Rev. Lett. **116**, 183901 (2016).

[32] G. Lopez-Galmiche, Z. S. Eznaveh, M. A. Eftekhar, J. A. Lopez, L. G. Wright, F. Wise, D. Christodoulides, and R. A. Correa, Visible supercontinuum generation in a graded index multimode fiber pumped at 1064 nm, Opt. Lett. **41**, 2553 (2016).

[33] H. E. Lopez-Aviles, F. O. Wu, Z. S. Eznaveh, M. A. Eftekhar, F. Wise, R. A. Correa, and D. N. Christodoulides, A system-

atic analysis of parametric instabilities in nonlinear parabolic multimode fibers, APL Photonics **4**, 022803 (2019).
[34] L. G. Wright, D. N. Christodoulides, and F. W. Wise, Spatiotemporal mode-locking in multimode fiber lasers, Science **358**, 94 (2017).
[35] L. G. Wright, P. Sidorenko, H. Pourbeyram, Z. M. Ziegler, A. Isichenko, B. A. Malomed, C. R. Menyuk, D. N. Christodoulides, and F. W. Wise, Mechanisms of spatiotemporal mode-locking, Nat. Phys. **16**, 565 (2020).
[36] W. H. Renninger and F. W. Wise, Optical solitons in graded-index multimode fibres, Nat. Commun. **4**, 1719 (2013).
[37] Z. Liu, L. G. Wright, D. N. Christodoulides, and F. W. Wise, Kerr self-cleaning of femtosecond-pulsed beams in graded-index multimode fiber, Opt. Lett. **41**, 3675 (2016).
[38] K. Krupa, A. Tonello, B. M. Shalaby, M. Fabert, A. Barthélémy, G. Millot, S. Wabnitz, and V. Couderc, Spatial beam self-cleaning in multimode fibres, Nat. Photon. **11**, 237 (2017).
[39] E. T. Jaynes, Information theory and statistical mechanics, Phys. Rev. **106**, 620 (1957).
[40] R. K. Pathria and P. D. Beale, *Statistical Mechanics*, 3rd ed. (Elsevier, Oxford, 2011).
[41] F. O. Wu, A. U. Hassan, and D. N. Christodoulides, Thermodynamic theory of highly multimoded nonlinear optical systems, Nat. Photon. **13**, 776 (2019).
[42] M. Parto, F. O. Wu, P. S. Jung, K. Makris, and D. N. Christodoulides, Thermodynamic conditions governing the optical temperature and chemical potential in nonlinear highly multimoded photonic systems, Opt. Lett. **44**, 3936 (2019).
[43] K. G. Makris, F. O. Wu, P. S. Jung, and D. N. Christodoulides, Statistical mechanics of weakly nonlinear optical multimode gases, Opt. Lett. **45**, 1651 (2020).
[44] M. Ferraro, F. Mangini, F. O. Wu, M. Zitelli, D. N. Christodoulides, and S. Wabnitz, Calorimetry of Photon Gases in Nonlinear Multimode Optical Fibers, Phys. Rev. X **14**, 021020 (2024).
[45] N. K. Efremidis and D. N. Christodoulides, Thermodynamic optical pressures in tight-binding nonlinear multimode photonic systems, Commun. Phys. **5**, 2399 (2022).
[46] L. G. Wright, F. O. Wu, D. N. Christodoulides, and F. W. Wise, Physics of highly multimode nonlinear optical systems, Nat. Phys. **18**, 1018 (2022).
[47] H. Pourbeyram, P. Sidorenko, F. O. Wu, N. Bender, L. Wright, D. N. Christodoulides, and F. Wise, Direct observations of thermalization to a Rayleigh-Jeans distribution in multimode optical fibres, Nat. Phys. **18**, 685 (2022).
[48] Q. Zhong, F. O. Wu, A. U. Hassan, R. El-Ganainy, and D. N. Christodoulides, Universality of light thermalization in multimoded nonlinear optical systems, Nat. Commun. **14**, 370 (2023).
[49] K. Baudin, J. Garnier, A. Fusaro, N. Berti, C. Michel, K. Krupa, G. Millot, and A. Picozzi, Observation of light thermalization to negative-temperature Rayleigh-Jeans equilibrium states in multimode optical fibers, Phys. Rev. Lett. **130**, 063801 (2023).
[50] A. L. Marques Muniz, F. O. Wu, P. S. Jung, M. Khajavikhan, D. N. Christodoulides, and U. Peschel, Observation of photon-photon thermodynamic processes under negative optical temperature conditions, Science **379**, 1019 (2023).
[51] J. Klaers, F. Vewinger, and M. Weitz, Thermalization of a two-dimensional photonic gas in a 'white wall' photon box, Nat. Phys. **6**, 512 (2010).
[52] J. Klaers, J. Schmitt, F. Vewinger, and M. Weitz, Bose-Einstein condensation of photons in an optical microcavity, Nature (London) **468**, 545 (2010).
[53] A. Chiocchetta, P. É. Larré, and I. Carusotto, Thermalization and Bose-Einstein condensation of quantum light in bulk nonlinear media, Europhys. Lett. **115**, 24002 (2016).
[54] J. Bloch, I. Carusotto, and M. Wouters, Non-equilibrium Bose-Einstein condensation in photonic systems, Nat. Rev. Phys. **4**, 470 (2022).
[55] L. Zanaglia, J. Garnier, S. Rica, R. Kaiser, S. Wabnitz, C. Michel, V. Doya, and A. Picozzi, Bridging Rayleigh-Jeans and Bose-Einstein condensation of a guided fluid of light with positive and negative temperatures, Phys. Rev. A **110**, 063530 (2024).
[56] A. Y. Ramos, C. Shi, L. J. Fernández-Alcázar, D. N. Christodoulides, and T. Kottos, Theory of localization-hindered thermalization in nonlinear multimode photonics, Commun. Phys. **6**, 189 (2023).
[57] A. Kurnosov, L. J. Fernández-Alcázar, A. Ramos, B. Shapiro, and T. Kottos, Optical kinetic theory of nonlinear multimode photonic networks, Phys. Rev. Lett. **132**, 193802 (2024).
[58] M. Ramezani, M. Golshani, and A. T. Rezakhani, Fluctuation relation for heat exchange in Markovian open quantum systems, Phys. Rev. E **97**, 042101 (2018).
[59] A. M. Timpanaro, G. Guarnieri, J. Goold, and G. T. Landi, Thermodynamic uncertainty relations from exchange fluctuation theorems, Phys. Rev. Lett. **123**, 090604 (2019).
[60] J. D. Joannopoulos, P. R. Villeneuve, and S. Fan, Photonic crystals, Solid State Commun. **102**, 165 (1997).
[61] D. N. Christodoulides, F. Lederer, and Y. Silberberg, Discretizing light behaviour in linear and nonlinear waveguide lattices, Nature (London) **424**, 817 (2003).
[62] J. C. Knight, Photonic crystal fibres, Nature (London) **424**, 847 (2003).
[63] Y. Akahane, T. Asano, B.-S. Song, and S. Noda, High-Q photonic nanocavity in a two-dimensional photonic crystal, Nature (London) **425**, 944 (2003).
[64] P. Russell, Photonic crystal fibers, Science **299**, 358 (2003).
[65] C. López, Materials aspects of photonic crystals, Adv. Mater. **15**, 1679 (2003).
[66] F. Poletti and P. Horak, Description of ultrashort pulse propagation in multimode optical fibers, J. Opt. Soc. Am. B **25**, 1645 (2008).
[67] A. Mafi, Pulse propagation in a short nonlinear graded-index multimode optical fiber, J. Lightwave Technol. **30**, 2803 (2012).
[68] H. Pourbeyram, G. P. Agrawal, and A. Mafi, Stimulated Raman scattering cascade spanning the wavelength range of 523 to 1750 nm using a graded-index multimode optical fiber, Appl. Phys. Lett. **102**, 201107 (2013).
[69] See Supplemental Material at http://link.aps.org/supplemental/10.1103/PhysRevResearch.7.013084 for details about optical entropy, optical temperature, and chemical potential; the relation between dimensionless quantities and physical quantities; the derivation of the quantum master equation; and the convergence behaviors of the infinite matrix.

[70] S. Braun, J. P. Ronzheimer, M. Schreiber, S. S. Hodgman, T. Rom, I. Bloch, and U. Schneider, Negative absolute temperature for motional degrees of freedom, Science **339**, 52 (2013).
[71] K. M. Frahm and D. L. Shepelyansky, Nonlinear perturbation of random matrix theory, Phys. Rev. Lett. **131**, 077201 (2023).
[72] S. Datta and M. P. Anantram, Steady-state transport in mesoscopic systems illuminated by alternating fields, Phys. Rev. B **45**, 13761 (1992).
[73] J. E. Subotnik, T. Hansen, M. A. Ratner, and A. Nitzan, Nonequilibrium steady state transport via the reduced density matrix operator, J. Chem. Phys. **130**, 144105 (2009).
[74] U. Peskin, An introduction to the formulation of steady-state transport through molecular junctions, J. Phys. B: At. Mol. Opt. Phys. **43**, 153001 (2010).
[75] J.-S. Wang, B. K. Agarwalla, and H. Li, Transient behavior of full counting statistics in thermal transport, Phys. Rev. B **84**, 153412 (2011).
[76] B. K. Agarwalla, B. Li, and J.-S. Wang, Full-counting statistics of heat transport in harmonic junctions: Transient, steady states, and fluctuation theorems, Phys. Rev. E **85**, 051142 (2012).
[77] G.-M. Tang and J. Wang, Full-counting statistics of charge and spin transport in the transient regime: A nonequilibrium Green's function approach, Phys. Rev. B **90**, 195422 (2014).
[78] B. K. Agarwalla, J.-H. Jiang, and D. Segal, Full counting statistics of vibrationally assisted electronic conduction: Transport and fluctuations of thermoelectric efficiency, Phys. Rev. B **92**, 245418 (2015).
[79] J.-S. Wang, J. Peng, Z.-Q. Zhang, Y.-M. Zhang, and T. Zhu, Transport in electron-photon systems, Front. Phys. **18**, 43602 (2023).
[80] H. Li, B. K. Agarwalla, and J.-S. Wang, Cumulant generating function formula of heat transfer in ballistic systems with lead-lead coupling, Phys. Rev. B **86**, 165425 (2012).
[81] M. Paulsson and S. Datta, Thermoelectric effect in molecular electronics, Phys. Rev. B **67**, 241403(R) (2003).
[82] G. J. Snyder and T. S. Ursell, Thermoelectric efficiency and compatibility, Phys. Rev. Lett. **91**, 148301 (2003).
[83] M. Hatami, G. E. W. Bauer, Q. Zhang, and P. J. Kelly, Thermoelectric effects in magnetic nanostructures, Phys. Rev. B **79**, 174426 (2009).
[84] J.-H. Jiang, M. Kulkarni, D. Segal, and Y. Imry, Phonon thermoelectric transistors and rectifiers, Phys. Rev. B **92**, 045309 (2015).
[85] X.-D. Chen, F.-L. Zhao, M. Chen, and J.-W. Dong, Valley-contrasting physics in all-dielectric photonic crystals: Orbital angular momentum and topological propagation, Phys. Rev. B **96**, 020202(R) (2017).
[86] J. Kurchan, Fluctuation theorem for stochastic dynamics, J. Phys. A: Math. Gen. **31**, 3719 (1998).
[87] R. J. Harris and G. M. Schütz, Fluctuation theorems for stochastic dynamics, J. Stat. Mech. (2007) P07020.
[88] U. Harbola, M. Esposito, and S. Mukamel, Statistics and fluctuation theorem for boson and fermion transport through mesoscopic junctions, Phys. Rev. B **76**, 085408 (2007).
[89] M. Esposito, U. Harbola, and S. Mukamel, Nonequilibrium fluctuations, fluctuation theorems, and counting statistics in quantum systems, Rev. Mod. Phys. **81**, 1665 (2009).
[90] J.-F. Chen and H. T. Quan, Hierarchical structure of fluctuation theorems for a driven system in contact with multiple heat reservoirs, Phys. Rev. E **107**, 024135 (2023).
[91] C. Jarzynski, Nonequilibrium equality for free energy differences, Phys. Rev. Lett. **78**, 2690 (1997).
[92] O. P. Saira, Y. Yoon, T. Tanttu, M. Möttönen, D. V. Averin, and J. P. Pekola, Test of the Jarzynski and Crooks fluctuation relations in an electronic system, Phys. Rev. Lett. **109**, 180601 (2012).
[93] S. An, J.-N. Zhang, M. Um, D. Lv, Y. Lu, J. Zhang, Z.-Q. Yin, H. T. Quan, and K. Kim, Experimental test of the quantum Jarzynski equality with a trapped-ion system, Nat. Phys. **11**, 193 (2014).
[94] G. E. Crooks, Entropy production fluctuation theorem and the nonequilibrium work relation for free energy differences, Phys. Rev. E **60**, 2721 (1999).
[95] K. Zhang, X. Wang, Q. Zeng, and J. Wang, Conditional entropy production and quantum fluctuation theorem of dissipative information: Theory and experiments, PRX Quantum **3**, 030315 (2022).
[96] R. Sharma, T. P. Simula, and A. J. Groszek, Fluctuation theorem anomaly in a point-vortex fluid, Phys. Rev. A **110**, 013321 (2024).
[97] A. C. Barato and U. Seifert, Thermodynamic uncertainty relation for biomolecular processes, Phys. Rev. Lett. **114**, 158101 (2015).
[98] J. M. Horowitz and T. R. Gingrich, Thermodynamic uncertainty relations constrain non-equilibrium fluctuations, Nat. Phys. **16**, 15 (2020).
[99] Y. Hasegawa, Thermodynamic uncertainty relation for general open quantum systems, Phys. Rev. Lett. **126**, 010602 (2021).
[100] J. Lu, Z. Wang, J. Peng, C. Wang, J.-H. Jiang, and J. Ren, Geometric thermodynamic uncertainty relation in a periodically driven thermoelectric heat engine, Phys. Rev. B **105**, 115428 (2022).